

Accepted to ApJ 4/7/06.

Laboratory Testing of a Lyot Coronagraph Equipped with an Eighth-Order Notch Filter Image Mask

Justin R. Crepp, Jian Ge, Andrew D. Vanden Heuvel, Shane P. Miller

*Astronomy Department, University of Florida
211 Bryant Space Science Center, P.O. Box 112055
Gainesville, FL 32611-2055*

`jcrepp@astro.ufl.edu, jge@astro.ufl.edu, avh@astro.ufl.edu,
smiller@astro.ufl.edu`

Marc J. Kuchner

*Exoplanets & Stellar Astrophysics Laboratory
NASA - Goddard Space Flight Center
Greenbelt, MD 20771*

`marc.kuchner@nasa.gov`

ABSTRACT

We have built a series of notch filter image masks that make the Lyot coronagraph less susceptible to low-spatial-frequency optical aberrations. In this paper, we present experimental results of their performance in the lab using monochromatic light. Our tests show that these “eighth-order” masks are resistant to tilt and focus alignment errors, and can generate contrast levels of 2×10^{-6} at $3 \lambda/D$ and 6×10^{-7} at $10 \lambda/D$ without the use of corrective optics such as deformable mirrors. This work supports recent theoretical studies suggesting that eighth-order masks can provide the Terrestrial Planet Finder Coronagraph with a large search area, high off-axis throughput, and a practical requisite pointing accuracy.

Subject headings: extrasolar planets — high contrast imaging — coronagraphy — terrestrial planet finder — circumstellar matter

1. INTRODUCTION

A coronagraph is an instrument that controls the diffracted light from a bright astrophysical object in order to image faint off-axis features in its immediate vicinity. Future space-based missions, such as the Terrestrial Planet Finder (TPF) mission, will use a stellar coronagraph to search for Earth-like planets orbiting in the habitable zone of nearby stars

(Ford et al. 2004). Demonstrating this technology requires suppressing broadband visible starlight by more than a factor of $\sim 10^{10}$ only a few diffraction widths from the telescope optical axis. In this paper, we report on progress towards achieving this goal in the lab with a Lyot coronagraph that is equipped with an “eighth-order” notch filter image mask.

The Lyot coronagraph consists of an entrance aperture, an image mask, a field stop, and a detector (Lyot 1939). Light entering the coronagraph is focused onto the mask in the first image plane. If the telescope is pointed accurately, most of the starlight is occulted by the mask, while off-axis sources suffer little attenuation. The light is then diffracted to a pupil plane, the Lyot plane, where a stop is used to block the remaining starlight (Fig. 1).

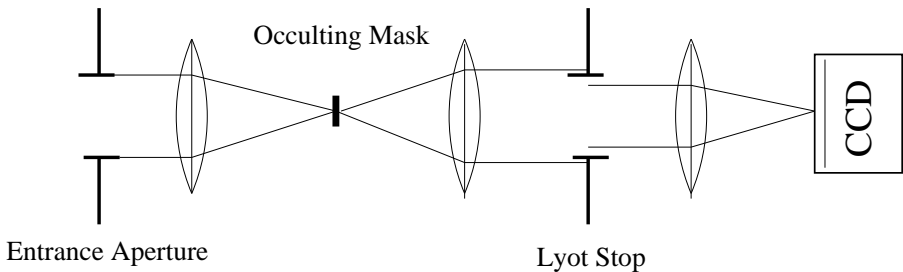


Fig. 1.— Optical layout of a transmissive Lyot coronagraph without wavefront correction. See Sivaramakrishnan et al. 2001 for a first-order theory description of how light interacts with the optical elements.

In the Fraunhofer diffraction regime, perfect elimination of on-axis light can be achieved with a band-limited image mask (Kuchner & Traub 2002). Band-limited masks are smooth graded masks that consist of only a limited range of low-spatial-frequencies. They operate by placing all of the diffracted light from a point source outside the edges of the Lyot stop. In the absence of scattered light and aberrations, the combination of the mask and optimized stop completely removes on-axis light, creating infinite dynamic range. The light from dim off-axis sources, such as sub-stellar companions or debris disks, penetrates the Lyot stop and forms an image at the detector.

Notch filter masks offer the same performance as band-limited masks, but have more design freedom (Kuchner & Spergel 2003). By transmitting power at high-spatial-frequencies, that diffract light well outside of the Lyot stop opening, notch filter masks afford the construction of sampled graded, sampled binary, and smooth binary masks. Binary masks are everywhere either completely opaque or perfectly transmissive.

Eighth-order masks are the first group in a large family of band-limited and notch filter masks, called “high-order” masks, that trade inner-working-angle (IWA) and Lyot stop throughput for resistance to aberrations (Kuchner, Crepp, & Ge 2005, hereafter KCG05). To demonstrate some of these properties in practice, we have built and tested several eighth-order notch filter masks. The results of our study are presented with the following: first, we discuss the advantages of using a high-order image mask for coronagraphy (§2); then, we describe the designs of the masks we have built (§3), and our experimental setup and techniques (§4); finally, we make direct comparisons between the eighth-order masks and a

fourth-order mask, which is used as an experimental control, by testing their sensitivity to tilt and focus aberrations (§5).

2. HIGH-ORDER IMAGE MASKS

The “order” of an image mask describes the intensity transmission of the mask near the optical axis. High-order masks have a broad central opaque region, and transmit less light near the optical axis than lower-order masks. To establish some notation, we define the order explicitly as: the exponent of the first term in the squared modulus of the expansion of the low-frequency part of the mask amplitude transmission, $\hat{M}(r)$, with respect to distance from the optical axis, r , where $r \ll \lambda_{min}/D$. For example, the $\hat{M}(r) = \sin^2(\alpha r)$ band-limited mask is fourth-order: $|\hat{M}(\alpha r)|^2 \sim (\alpha r)^4$, where α is a constant that controls the coronagraph’s bandwidth, IWA, and Lyot stop throughput. Since band-limited masks do not explicitly manipulate the phase of light in theory (which provides excellent broadband performance), they have symmetric transmission profiles. As a result, the order of masks increases by increments of four, starting with fourth-order (see Kuchner 2004). The next higher-order mask function in the sequence, an eighth-order mask, is simply a linear combination of two fourth-order mask functions weighted such that the quadratic term in the amplitude transmission cancels. This forces the quartic term, and subsequent low-order cross-terms, in the intensity transmission to zero.

KCG05 show that the following equations describe the amplitude transmission of two series of eighth-order band-limited image masks:

$$\hat{M}_{BL}(r) = N \left[\frac{3n-1}{3n} - \text{sinc}^n(\alpha r/n) + \left(\frac{1}{3n} \right) \cos(\alpha r) \right], \quad (1)$$

and

$$\hat{M}_{BL}(r) = N \left[\frac{l-m}{l} - \text{sinc}^l(\alpha r/l) + \frac{m}{l} \text{sinc}^m(\alpha r/m) \right], \quad (2)$$

where N is a normalization constant, and n , m , and l are positive integers. For a given IWA, the mask functions in Equation 1 generally yield higher Lyot stop throughput, while the mask functions in Equation 2 have less off-axis attenuation. Additionally, there is a trade-off between the Lyot stop throughput and image-plane off-axis attenuation as n , m , and l increase: large exponents yield lower Lyot stop throughput but less ‘ringing’. We use these exponents to refer to the various combinations available for constructing eighth-order masks. For instance, the $m = 1$, $l = 2$ mask combines the $1 - \text{sinc}()$ and $1 - \text{sinc}^2()$ fourth-order band-limited functions, and an $n = 3$ mask combines the $1 - \text{sinc}^3()$ and $1 - \cos()$ functions. All high-order masks, including notch filter masks - both sampled and smooth -, use fourth-order band-limited mask functions as a basis set for design.

The next higher-order masks that manipulate the amplitude of starlight and not the phase are twelfth-order, sixteenth-order, twentieth-order, and so on. Shaklan & Green 2005 (hereafter SG05) have shown with numerical simulations that the order of the mask is di-

rectly related to its sensitivity to low-spatial-frequency aberrations: higher-order masks significantly reduce light leakage due to low-spatial-frequency aberrations, and can generate better contrast than lower-order masks at a given aberration level.¹

When compared to fourth-order masks, eighth-order masks relax pointing requirements by almost an order of magnitude (KCG05). They relax wavefront error requirements for focus, astigmatism, coma, and trefoil by two orders of magnitude, and help to reduce leakage due to spherical aberration and various polarization effects (SG05). Eighth-order masks can also generate regions of high contrast around stars of appreciable angular size (KCG05, Crepp & Ge 2006, in preparation). However, increasing the order of the mask requires decreasing the Lyot stop throughput, when the IWA is fixed. Choosing an optimal mask depends upon the application.

The current mission goals and observing strategy for the TPF-C are to generate better than 10^{-10} contrast at angular separations as close as $\sim 4\lambda_{max}/D$ from targeted main-sequence F, G, and K stars within the solar neighborhood. KCG05 and SG05 suggest that an $m = 1, l = 3$ eighth-order mask can meet these criterion, offering a good compromise between Lyot stop throughput, off-axis attenuation, and aberration sensitivity. However, if the mission is altered or expanded to search more luminous stars, such as sub-giant or red giant stars that have more distant and extended habitable zones (Lopez, Schneider, & Danchi 2005), the IWA can be increased. In this situation, a higher-order mask could be used to relax the overall aberration sensitivity of the instrument and reduce leakage due to the larger stellar angular sizes, while maintaining a high Lyot stop throughput. For example, a twelfth-order linear mask composed of $1 - \text{sinc}()$, $1 - \text{sinc}^2()$, and $1 - \text{sinc}^8()$ functions can be designed to have an IWA of $10\lambda_{max}/D$ with a Lyot stop throughput of $\sim 64\%$ and very little off-axis attenuation, over the entire TPF-C bandwidth.

From the ground, higher-order masks can be used to compensate for systems with low-order aberrations left uncorrected by the adaptive optics (AO) system, possibly those introduced by telescope flexure, for example. However, the Lyot stop throughput is often severely restricted by a telescope central obstruction, placing limits on the order of the mask that can be implemented. We calculate that a telescope with a central obstruction of width $0.36 D$, such as the Hale 200" at Palomar, can achieve $\sim 16\%$ Lyot stop throughput when operating at $2.2\mu m$ with an $m = 1, l = 3$ 8th-order radial mask with an IWA of 600 mas, and that the throughput goes to zero once the bandwidth is increased beyond $\sim 20\%$. With the same parameters, a twelfth-order radial mask would have zero throughput even with monochromatic light, regardless of the composite functions. In practice, the size of the Lyot stop may be reduced further compared to these ideal cases.

¹This technique of generating broad central ‘nulls’ is adopted from interferometry; by adding telescopes to an array and forming certain configurations, sets of nulling interferometers, each with a π phase shift at one arm, can be combined to form larger nulling interferometers composed of N dishes (Rouan 2004).

3. MASK DESIGN & FABRICATION

We have manufactured four binary notch filter image masks using *e*-beam lithography: one fourth-order mask and three eighth-order masks. These masks represent a second generation of technology development, where we have improved upon the prototype mask presented in Debes et al. 2004. In the following, we briefly describe our design strategy and nanofabrication techniques.

The base structure used to mechanically support the opaque portions of the masks is a 0.7 mm thick piece of Boroaluminosilicate glass with a scratch/dig of 20/10. A 270 nm thick layer of Chromium serves as the on-axis occulting material, and was deposited onto one side of the glass using a Semicore *e*-gun evaporator. Small structures were then dry-etched from the Chrome layer with an applied materials cluster tool using a high density decoupled plasma composed of Argon, Chlorine, and Oxygen. No anti-reflection coating was applied. Figure 2 shows a photo of the substrate containing all of the designs.

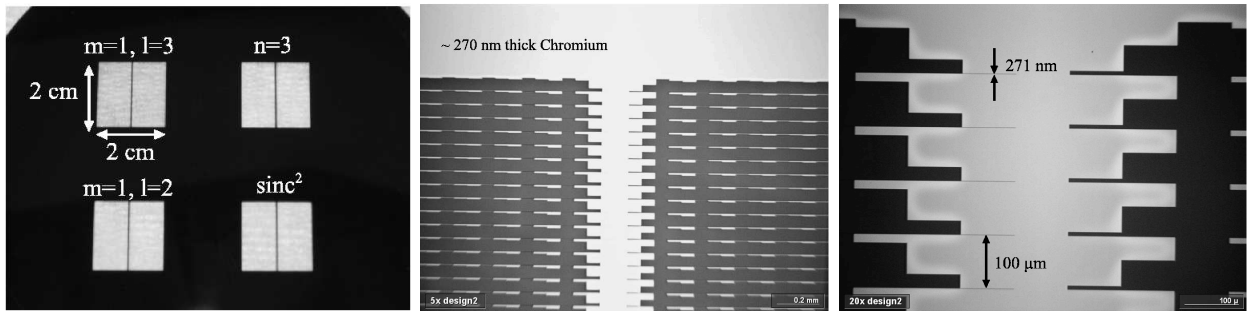


Fig. 2.— The four linear binary notch filter image masks (left), and optical microscope false color images of the $m = 1$, $l = 2$ eighth-order mask at 5x magnification (middle) and 20x magnification (right). The dark areas in the microscope images are transparent; this is where the Chrome has been etched away. The spacing between stripes and the spacing between samples is $\lambda_{min} f/\# = 100 \mu m$.

Each mask is designed for an $f/163$ or slower beam with a 40 nm bandwidth centered on the $\lambda = 632.8$ nm HeNe laser source. The focal ratio of the system is large to facilitate the fabrication of small features in the masks. The physical size or extent of the masks are 2 cm to a side. Although truncation sets an outer-working-angle and degrades contrast, notch filter masks can easily be manufactured large enough to ensure that these effects do not place significant constraints on the search area and are not the dominant source of error. Notch filter masks can be designed to have an azimuthally symmetric search area; however, we have chosen to make linear masks so that the effective opacity changes in only one direction. This property simplified the testing of their response to pointing errors. The FWHM of the image masks (i.e. $2 \times$ IWA) were designed to be roughly equivalent such that fair comparisons of their performance could be made (Table 1). Aime 2005 suggests that the mask equivalent-width serves as a better proxy for making such comparisons; the authors note that the FWHM value differs from the equivalent-width value by $\lesssim 1\%$ for each of the individual masks presented here.

Linear binary masks consist of vertically repeating parallel stripes, where band-limited or notch filter functions describe the curves in each stripe (Kuchner & Spergel 2003). We have made binary masks using the notch filter functions, because sampling makes the intricate features near the optical axis a part of the design, and not the result of the finite resolution of the lithography machine. In general, the sampling is not symmetric (Fig. 2). The low-frequency amplitude transmission of the eighth-order masks follow Equations 1 and 2, where r is replaced with x .

The smallest features in a mask are often found near the optical axis. Their size depends upon both the IWA and bandwidth, among other parameters. Generally, as the IWA improves (i.e. gets smaller), the size of the smallest features in the mask increases, and as the bandwidth widens, the size of the smallest features decreases. If the IWA is too large or the bandwidth too wide, the smallest features may be too small to build.

An additional constraint is that the minimum feature sizes should not be smaller than the thickness of the opaque material. This helps to minimize the waveguide effects associated with binary masks, and other vector electromagnetic effects that can degrade contrast, especially with broadband light. Lay et al. 2005 describe some of these potential limiting factors for the TPF-C mission, and suggest several alternatives for compensation; one of which includes dramatically increasing the focal ratio at the mask ($> f/60$), as was done in this experiment. This design strategy was also implemented in the Debes et al. 2004 experiment for similar reasons.

Minimum feature size requirements - both practical and theoretical - limited our ability to make eighth-order masks with high Lyot stop throughput. In theory, eighth-order masks can achieve $\sim 50\%$ Lyot stop throughput with IWAs of $\sim 4\lambda_{max}/D$. Our masks were *designed* however to achieve only $\sim 20\%$ throughput at most, because we were restricted to making features larger than the thickness of the Chrome; the smallest feature size in each of the eighth-order masks is ~ 270 nm, whereas the smallest feature size in the fourth-order mask is 7119 nm. To increase the throughput, we would have to increase the $f/\#$, decrease the bandwidth, or decrease the thickness of the Chrome. Clearly the focal ratio is already large and the bandwidth is already narrow. Also, we show in §5 that increasing the thickness of the Chrome is the most notable improvement we have made upon the mask presented in Debes et al. 2004. Thus, future mask development will necessarily involve using a material that is intrinsically more opaque at visible wavelengths, such as Aluminum (Semaltianos 2001; Lay et al. 2005). This will enable the fabrication of masks that have more opacity and smaller minimum features sizes.

The equations describing the exact structure of linear, binary, sampled eighth-order notch filter image masks are derived in KCG05. Table 1 displays the relevant quantities for our designs, using the same notation (except in KCG05 $f/\# = f$). For each mask, sampling began at a horizontal distance of $x = \zeta_0 \lambda_{min} f/\#$ from the optical axis.

Mask	sinc^2	$n = 3$	$m = 1, l = 2$	$m = 1, l = 3$
order	4th ^a	8th	8th	8th
IWA/(λ_{max}/D)	2.350	2.372	2.332	2.356
ϵ	0.488	0.674	0.716	0.759
N	1.01444077	0.99098830	1.93640370	1.47114548
$\hat{M}_0{}_A$	0.01423518	0.07833984	0.05989364	0.06702707
$\hat{M}_0{}_B$	—	0.01803281	0.03028228	0.02278117
C	—	-0.25123206	-0.51959437	-0.35644301
ζ_0	0.28800972	0.25875213	0.25877876	0.25874218
Smallest Feature	7119 nm	271 nm	270 nm	270 nm
Theoretical Throughput	40.4%	21.2%	17.4%	13.7%
Experimental Throughput	30.7%	15.7%	13.0%	10.4%

Table 1: Mask design parameters for a bandpass of 632.8 ± 20 nm. For an elliptical or circular primary mirror, the Lyot stop throughput of a linear mask is given by: $T = 1 - \frac{2}{\pi}[\epsilon\sqrt{1 - \epsilon^2} + \arcsin(\epsilon)]$, where $0 \leq \epsilon \leq 1$ is a dimensionless parameter that controls the width of the zones of diffracted starlight at the edges of the Lyot stop. We were able to achieve $\sim 75\%$ of the theoretical Lyot stop throughput for each mask in the experiment.

^aFourth-order masks have only one \hat{M}_0 and no C (KCG05).

4. EXPERIMENTAL SETUP

The design of the University of Florida coronagraphic testbed is that of a standard transmissive Lyot coronagraph without wavefront correction, as depicted in Figure 1, and similar to the setup described in Debes et al. 2004. “Starlight”, generated by a $\lambda = 632.8$ nm HeNe laser for monochromatic testing, passes first through a set of neutral density (ND) filters and is then focused by a microscope objective lens into a $4\ \mu\text{m}$ single-mode fiber for spatial filtering. The fiber exit-tip serves as a bright point source. This expanding beam, N.A. = 0.12, is collimated and then truncated by a circular ~ 3 mm diameter iris, simulating the primary mirror of an off-axis telescope. Optics downstream from the iris are high quality achromat doublets capable of handling future broadband tests. The first achromat, $f = 500$ mm, focuses the light onto the substrate containing all of the notch filter image masks. The substrate is mounted onto a precision x-y-z stage for fine adjustments. The light is then re-collimated by an identical achromat. In the Lyot plane, an optimized Lyot stop blocks the light diffracted by the mask at the location of the reimaged entrance pupil. The Lyot stop size is adjustable and takes the shape of the intersection of two overlapping circles, since the masks are linear. The remaining light is then focused onto an SBIG ST-2000XM CCD detector where images are taken for analysis. The images are sampled approximately $10\times$ more frequently than the Nyquist frequency with $7.4\ \mu\text{m}$ pixels. The analog-to-digital converter has a bit depth of 16, and the CCD has a factory quoted RMS read noise of $7.9\ e^-$. These sources of noise are always at least two orders of magnitude smaller than the measured contrast values when used in concert with our experimental techniques, which are

described in the following.

In order to measure contrast, we perform a comparison of images taken with and without the coronagraph in place. Due to the extreme contrast levels involved, we use a combination of the ND filters and the linearity of the CCD to calculate relative intensities and to generate high signal-to-noise ratio images in a reasonable amount of time. We first attenuate the laser light with the ND filters, which are placed upstream from the single-mode-fiber to ensure that their aberration effects are negated, and take an image of the star without the mask and without the Lyot stop in the optical train. Then, the mask and Lyot stop are inserted into place, and the ND filters are removed. In this final image, the intensity values at each pixel are divided by the average flux within the FWHM of the image of the star taken without the coronagraph, and normalized to the integration times and ND filters used. We define the resulting value, at each pixel, as the relative intensity. The contrast then is simply the relative intensity divided by the Lyot stop throughput and band-limited (i.e. low-frequency) part of the mask intensity transmission at that position. Figure 3 shows images of the star at various steps in the procedure. We could have chosen a less conservative definition of contrast by instead normalizing to the interpolated peak intensity of the imaged source, rather than the average flux within the FWHM (SG05); however, these two values differ by less than a factor of two. It is not necessary to add and remove the Lyot stop in order to measure contrast, but we find that doing so facilitates calculation of the off-axis throughput.

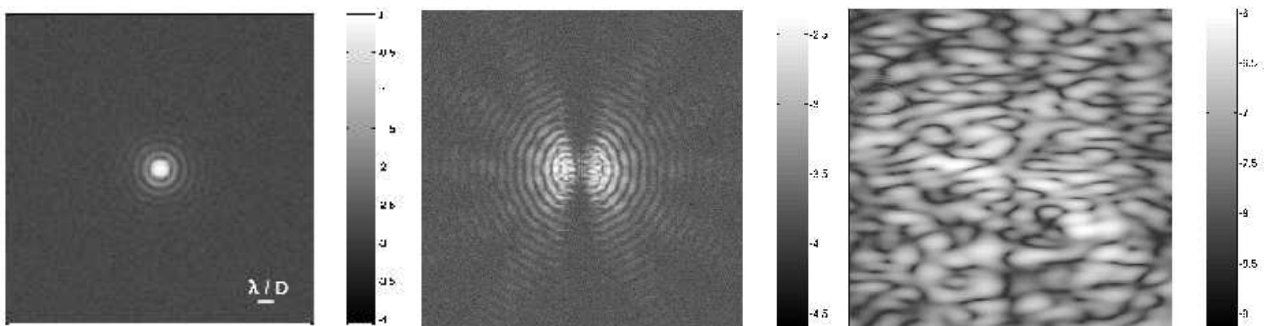


Fig. 3.— Laboratory images of the simulated star without the coronagraph (left), the $m = 1$, $l = 2$ mask aligned over the star (middle), and the star with both the mask and Lyot stop in place (right). Intensities are plotted on a logarithmic scale. The image of the star shows the angular size scale of the telescope. Speckles created by imperfections in the optics limit the dynamic range of the coronagraph creating a noise floor at the $\sim 10^{-7}$ level near the IWA. The contrast is calculated by dividing the relative intensity, shown in the image on the right and later in Fig. 4, by the Lyot stop throughput and mask intensity transmission; this accounts for the off-axis attenuation of the coronagraph.

Linear binary masks approximate band-limited masks only when the vertical angular size of the stripes in the mask are smaller than λ_{min}/D , the resolution of the telescope. To ensure that the masks diffract light appropriately, we increased the focal ratio of the system in the first image plane from the initial design of $f/\# = 163$ to $f/\# \approx 187$, by shrinking the size of the entrance aperture. This also resulted in an improvement of the masks' effective IWA by the same factor. The Lyot stop size was set conservatively to obtain $\sim 75\%$ of the

maximum theoretical throughput, so that small mis-alignments did not result in diffracted light leakage through the center of the stop onto the detector. Table 1 shows the designed IWAs before increasing the focal ratio, and the experimental Lyot stop throughput achieved.

5. RESULTS

5.1. Chrome Transmission & Relative Intensities

The performance of the prototype mask presented in Debes et al. 2004 was limited by the transmission of light directly through the Chromium occulting layer. In this study, we have increased the thickness of this layer from 105 nm to 270 nm. Using the transmission curve in Debes et al. 2004, we calculate that the peak transmission should improve from 7.5×10^{-4} to 9.2×10^{-9} . We measure a peak transmission of 2.3×10^{-8} . This is slightly worse than predicted, but opaque enough for this application nevertheless (Fig. 4). The discrepancy in these values can be understood by considering inhomogeneities in the thickness of the Chromium layers. A < 5 nm deviation in each makes up the difference. The contribution of transmission directly through the Chromium to the limiting contrast in this experiment is approximately one order of magnitude smaller than the scattered light floor near the IWA, and less so in the regions where the masks have little off-axis attenuation. A more demanding application, such as the TPF-C, would, of course, require a material with a higher opacity.

Figure 4 also shows a difference in the amount of light transmitted near the optical axis, $r \lesssim \lambda/D$, between the fourth-order mask and the eighth-order masks. This is evidence that the eighth-order masks are blocking more scattered light, simply because they are wider, and reducing the effects of low-order aberrations (we test this latter claim more carefully in §5.3). These properties are not seen as clearly in contrast curves, where, interior to the IWA, the intensity transmission of the mask controls the detection threshold.

5.2. Contrast Measurements

In a system dominated by scattered light, the relative intensities should scale according to the size of the Lyot stop. An equivalent statement is that in a system dominated by scattered light, the *contrast* should be *independent* of the Lyot stop size for a given mask (assuming, of course, that the Lyot stop is smaller than the diffracted light pattern in the Lyot plane). We find that the contrast generated by our masks is independent of the undersizing of the Lyot stop,² and that the coronagraph’s performance is limited by scattered light. The image plane speckles seen in Figure 3 are the result of wavefront distortions, created by imperfections in the optics. In practice, speckles can mimic and often overwhelm the light of dim companions.

²This is not the case when aberrations are added (§ 5.3).

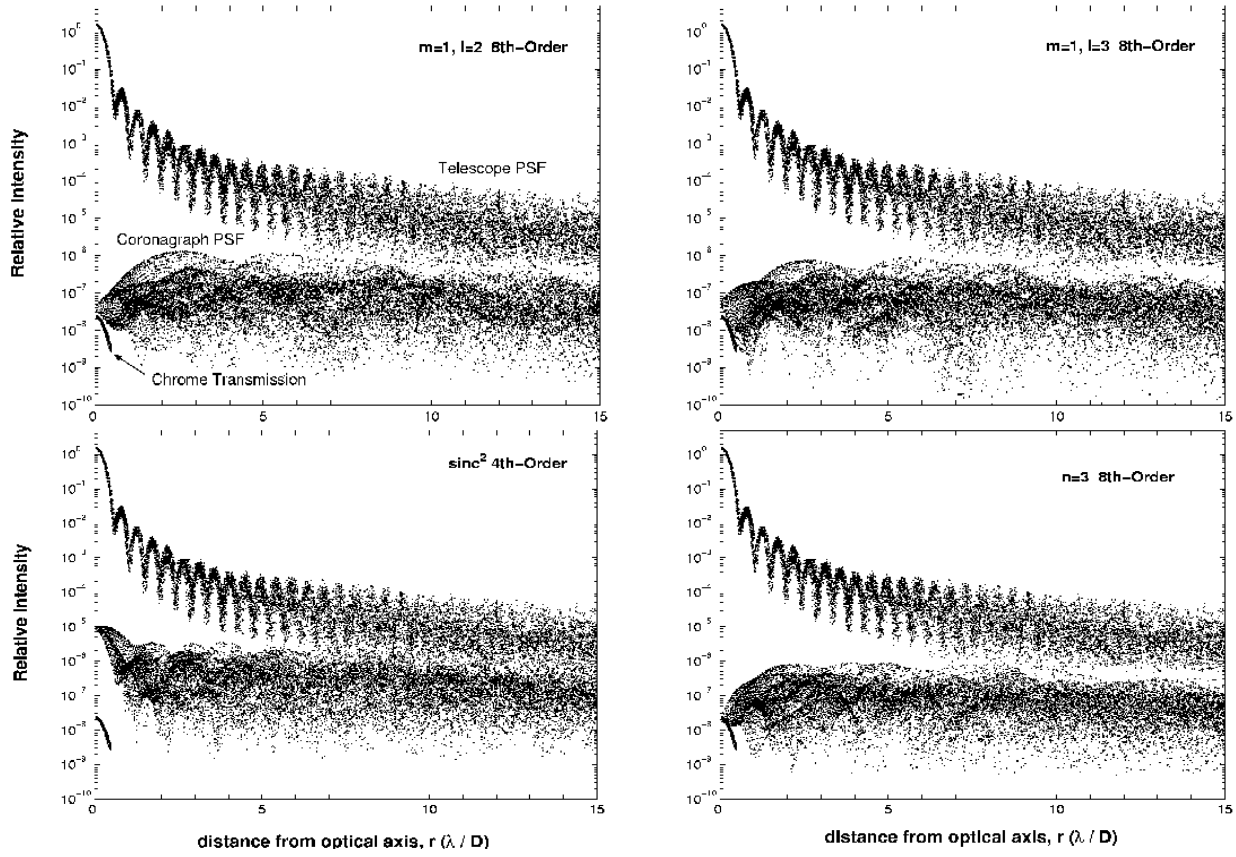


Fig. 4.— Telescope PSF, coronagraph PSF, and Chrome transmission for each mask using a circular entrance aperture. The Chrome transmission was measured at the center of the substrate. Inside the IWA, the eighth-order masks block more scattered light and reduce the effects of low-order aberrations. The thickness of the Chromium does not limit the performance of the coronagraph, but does transmit a non-negligible amount of light which contributes to the noise floor. Contrast is calculated by dividing the coronagraph PSF by the intensity transmission of the mask and the Lyot stop throughput.

We calculated contrast for pixels within a $10\lambda/D \times 30\lambda/D$ section across the center of the PSF by dividing the relative intensities by the Lyot stop throughput and band-limited part of the mask intensity transmission, $|\hat{M}(x)|^2$, at each position, x , the horizontal distance of pixels from the optical axis. That way, the direction in which the halo of speckles decreased in flux coincided with the direction of opacity change in the masks. We were able to achieve 2×10^{-6} contrast at $3\lambda/D$ and 6×10^{-7} contrast at $10\lambda/D$, as quoted in the abstract. In Figure 5, we plot the corresponding 3σ detection limits, where σ is defined as the standard deviation of the scattered light noise floor at a given location in the final image plane. The eighth-order masks reduce the amount of scattered light close to the optical axis, and slightly out-perform the fourth-order mask near the IWA as a result of their more steeply increasing intensity transmission in that region. The contrasts in the rest of the search area are essentially identical.

To calculate the Strehl ratio of our system, we compared a model of the Airy pattern

incident onto the mask with experimental data. We find that the Strehl ratio exceeds 98%. Combining this with the fact that the coronagraph is speckle dominated and the optical quality of our achromats are high (see §5.3), we conclude that the detection limits shown in Figure 5 represent the approximate deepest contrast that is achievable from the ground with current AO systems, using this type of coronagraph.

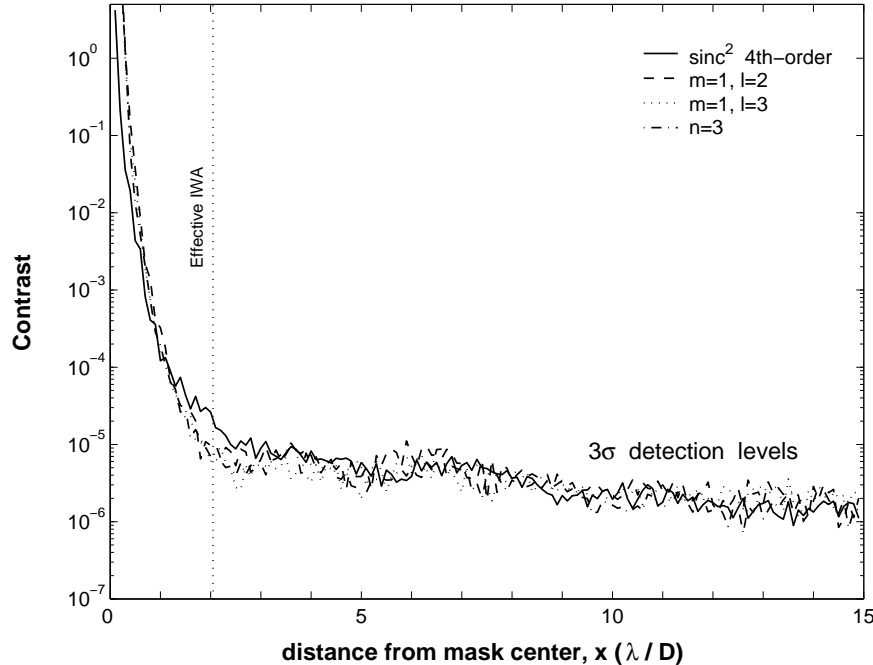


Fig. 5.— Experimental 3σ detection limits for each mask. The effective IWAs were calculated taking into consideration the change in focal ratio from the initial mask designs.

5.3. Aberration Sensitivity

We tested the tilt and focus aberration sensitivities of each mask by introducing small alignment errors to the substrate in the image plane. The results are shown in Figure 6, where we plot the contrast at $3\lambda/D$ as a function of the distance that the masks were displaced. The scattered light floor limits the dynamic range of the coronagraph at small aberration levels; in this regime, the masks generate contrasts to within a factor of two of one another, as shown in the previous section (Fig. 5). At large aberration levels, where diffracted light dictates the contrast, there is a clear dichotomy in the masks' behavior.

To measure the tilt aberration sensitivity of each mask, we moved the substrate laterally across the center of the image of the star in $5\ \mu\text{m}$ increments. We find that the eighth-order masks are easier to point than the fourth-order mask. To quantify this statement, we calculated the width of the pointing “sweet-spot” for each mask, where the contrast at $3\lambda/D$ is flat to within 2σ and limited by scattered light. The mean width of this zone for the eighth-order masks is $1.06 \pm 0.03\ \lambda/D$; the width of this zone for the fourth-order mask is $0.20 \pm 0.05\ \lambda/D$, a factor of ~ 5 smaller. With an 8 m telescope operating at $\lambda = 0.5\ \mu\text{m}$, these

tolerances correspond to pointing accuracies of 6.8 mas and 1.3 mas respectively. (Lloyd & Sivaramakrishnan 2005 discuss tip/tilt errors in Lyot coronagraphs in detail. For a practical application, see the description of the AEOS coronagraph by Lloyd et al. 2001.)

To measure the focus aberration sensitivity of each mask, we moved the substrate along the optical axis in logarithmic increments of 0.18 dex. With a similar analysis, we find that the eighth-order masks are also less susceptible than the fourth-order mask to focal misalignments. The eighth-order masks provide the same contrast as the fourth-order mask in a system with ~ 4 times as large an RMS wavefront error.

These results (Fig. 6) depend upon the amount of scattered light present in the system. If the scattered light levels were reduced, it would be possible to measure the response of the masks to smaller aberrations; the width of the tilt and focus sweet-spots would decrease as the contrast improves, and the relaxation ratios would change. KCG05 estimate that eighth-order masks should relax pointing requirements relative to fourth-order masks by a factor of ~ 6 in a system with no scattered light designed to achieve 10^{-10} contrast at $3\lambda/D$. SG05 have performed more careful calculations and predict an even larger relaxation ratio of 16 in the allowable tilt RMS wavefront deviation, when comparing eighth-order masks to fourth-order masks in an ideal system designed to achieve 10^{-12} contrast at $4\lambda/D$.

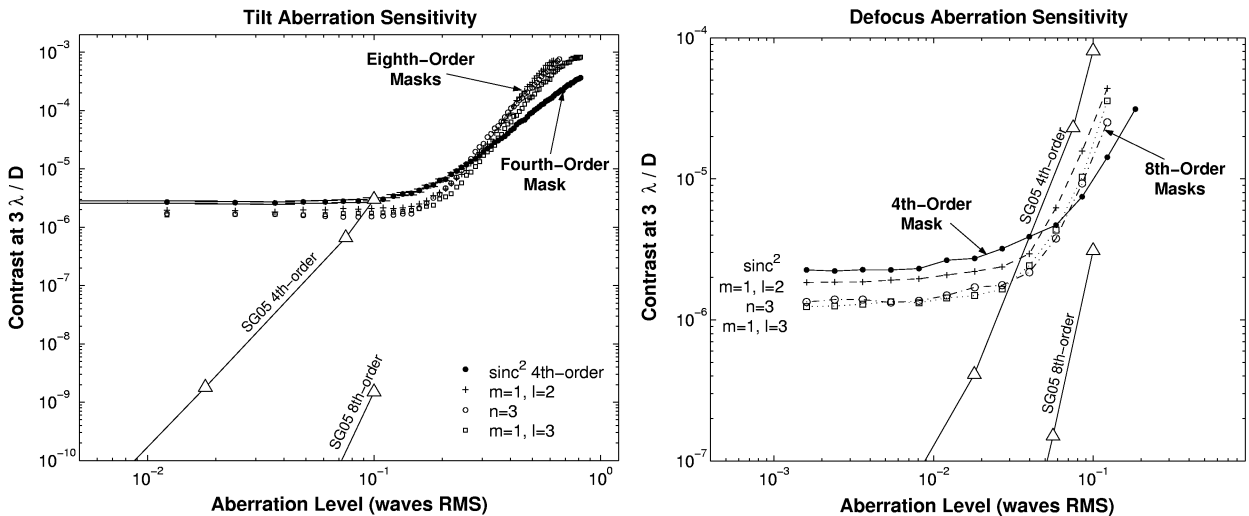


Fig. 6.— Coronagraph sensitivities to tilt (left) and focus (right) aberrations for each mask. The theoretical predictions of SG05 are over-plotted for comparison (see text). Scattered light prevented measurement of the diffracted light response of the masks at small aberration levels. Uncertainties in the measurements for the fourth-order mask are shown in the tilt graph; the errorbars are on the order of the size of the datapoints and representative for all of the experimental curves shown in both graphs. The focal ratio of our system was large enough to warrant tilt realignment for each focus datapoint, but not focus realignment for each tilt datapoint; this motivated the linear versus logarithmic measurement increments used for acquiring data.

For comparison, the SG05 theoretical tilt and focus curves are overplotted in Fig. 6 (the triangular data points); these represent the steepest possible slopes that can be achieved in

practice, since the model accounts only for diffraction. The general location of our experimental data are in good agreement with theory, and, to first order, simply adding a constant level of scattered light to the SG05 diffracted light curves recovers the eighth-order masks' experimental contrast to within the uncertainty of the measurements. The fourth-order mask however makes exception, by providing better contrast in practice than expected from theory. This apparent discrepancy is resolved by considering a subtle difference between the two studies: the Lyot stop size;³ the SG05 simulations maximize off-axis throughput by choosing the largest possible Lyot stop shape, whereas we have undersized the Lyot stop in this experiment by $\sim 25\%$ for each mask. In the presence of aberrations, the contrast of a band-limited mask depends upon the size of the Lyot stop. If the light diffracted in the Lyot plane due to aberrations is non-uniform and less intense near the optical axis, decreasing the size of the Lyot stop can improve contrast, at a cost of throughput and resolution (see Sivaramakrishnan et al. 2005). We find that the introduction of tilt and focus aberrations produces patterns in the Lyot plane that fit this description (Fig. 7), and that the undersizing of the Lyot stop is responsible for an enhanced resistance to aberrations. Furthermore, this effect is more pronounced with the fourth-order mask than the eighth-order mask, since low-order aberrations can be partially or completely filtered in the image plane before reaching the Lyot pupil.

It is a good assumption that the fourth- and eighth-order mask phase aberration contrast curves (Fig. 6) do not intersect at more than one point for a given aberration: the slope of a mask's dependence on *any* low-order Zernike mode is always at least as steep for eighth-order masks as it is for fourth-order masks (SG05). Since we see the intersection in both graphs in Fig. 6, we conclude that the eighth-order masks can achieve better contrast than the fourth-order mask when small levels of tilt and focus aberrations are present, even though this regime was not available for direct measurement in our experiment. At intermediate aberration levels, we do indeed see an improvement in contrast with the eighth-order masks. This is more evident with tilt, because the intersection between experimental curves occurs well above the scattered light floor.

Reducing the amount of scattered light in the coronagraph by approximately two orders of magnitude will enable a more reliable extrapolation of data to smaller aberrations with future work; however, polishing the optics with such precision is not feasible. The achromat doublets in this experiment are the same that were used in Debes et al. 2004, with rms surface roughnesses of $\lesssim 1$ nm on spatial frequency scales that correspond to the search area. A better technique to compensate for the scattered light present in the system at this level would be to implement a deformable mirror (e.g. Trauger et al. 2004).

³Other differences between this study and SG05 are: (1) we used a circular entrance aperture, instead of an elliptical entrance aperture, and (2) the contrast was measured at $3 \lambda/D$, instead of $4 \lambda/D$.

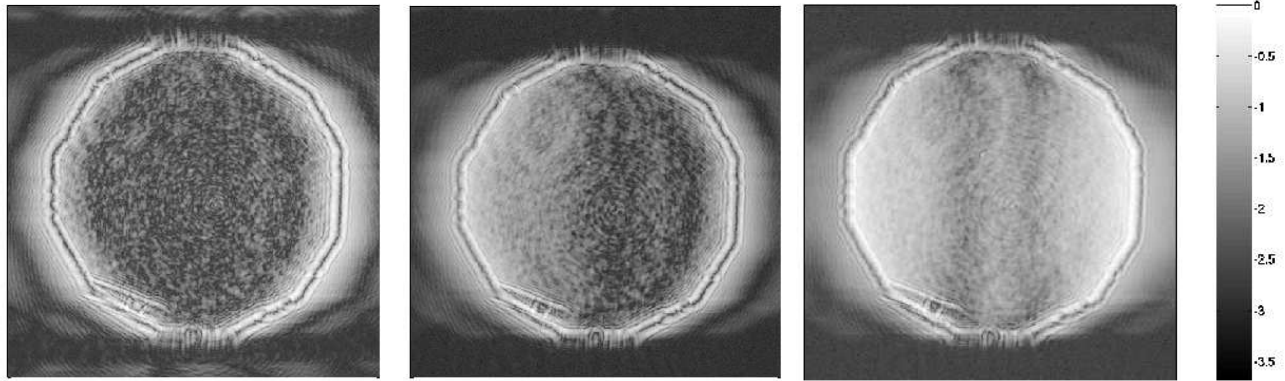


Fig. 7.— Characteristic Lyot plane images with optimum mask alignment (left), and 2×10^{-1} waves RMS tilt aberration (middle), and 9×10^{-2} waves RMS focus aberration (right) using the $m = 1, l = 2$ mask. Intensities are normalized to the peak intensity of the focus image and are on a logarithmic scale. Shrinking the Lyot stop can improve contrast when certain aberrations are present, as is the case here. These images can be compared to the analytic predictions in Fig. 3 of Sivaramakrishnan et al. 2005. Evidently, small amplitude tilt and focus phase aberrations produce a uniform leakage of light into the Lyot pupil interior. Although the aberrations presented here are rather large, aspects of both images appear to reflect this phenomena. More complicated processes such as cross-talk between induced and inherent aberrations as well as frequency-folding from mask construction errors also contribute to the Lyot pupil field, and can create an intensity gradient.

6. SUMMARY

We have built and tested three eighth-order notch filter masks and one fourth-order notch filter mask - each with the same IWA - to make a comparative study of low-spatial-frequency optical aberration sensitivities within the context of Lyot coronagraphy, using monochromatic light. We find that the eighth-order masks are less susceptible to the low-order aberrations of tilt and focus than the fourth-order mask: they provide the same contrast as the fourth-order mask in a system with either ~ 5 times as large a pointing error or ~ 4 times as large an RMS focus wavefront error. Additionally, the eighth-order masks show a stronger dependence to both tilt and focus at large aberration levels (i.e. a steeper slope), as predicted by theory. There was excellent agreement with our results and the SG05 numerical model, once the differences in each study were accounted for. We were unable to extrapolate our data to calculate the exact aberration levels necessary to achieve $\lesssim 10^{-10}$ contrast at the IWA because of the amount of scattered light in the system; doing so would require implementing a deformable mirror to reduce the scattered light levels by approximately two orders of magnitude. Transmission of light directly through the Chromium occulting layer accounted for $\sim 10\%$ of the noise floor at the IWA, but significantly less in the extended search area.

With “perfect” alignment, we find that all of the masks generate contrast levels of $\sim 2 \times 10^{-6}$ at $3 \lambda/D$ and $\sim 6 \times 10^{-7}$ at $10 \lambda/D$. In essence, the on-axis (‘stellar’) flux was

reduced by 7 orders of magnitude at the expense of attenuating off-axis light by a factor of $4 - 10$. Since our system is “diffraction limited” (i.e. $\gtrsim 80\%$ Strehl ratio), we conclude that the 3σ detection thresholds shown in Fig. 5 represent the approximate deepest contrast that is achievable from the ground with current AO, using this type of coronagraph.

The Lyot stop throughput penalty in switching from a fourth-order mask to an eighth-order mask was greatly exaggerated in this study, because of nanofabrication limitations. We were able to achieve $\sim 31\%$ Lyot stop throughput with the fourth-order mask and $\sim 10\% - 16\%$ with the eighth-order masks. With a material that is more opaque than Chrome at visible wavelengths, such as Aluminum, eighth-order masks will be able to reach their full potential in future experiments.

These results support the recent theoretical studies of Kuchner, Crepp, & Ge 2005 (KCG05) and Shaklan & Green 2005 (SG05) suggesting that eighth-order image masks can meet the demands of a space mission designed to image extrasolar terrestrial planets, such as the TPF-C, by providing the Lyot coronagraph with a large dynamic range, high off-axis throughput, a large search area, and resistance to low-spatial-frequency wavefront aberrations.

We thank Xiaoke Wan and Bo Zhao for their assistance in the lab, Lakshminarayan Hariharan for building the optimized Lyot stops, and Stuart Shaklan and John Debes for their helpful comments. We acknowledge support from the NSF with grants NSF AST-0451407 and AST-0451408, NASA with grants NNG05G321G and NNG05GR41G, the JPL TPF program, the UCF-UF SRI program, the University of Florida and Penn State. This research was also funded in part by a Grant-In-Aid of Research from the National Academy of Sciences, Administered by Sigma Xi, The Scientific Research Society.

REFERENCES

Aime, C. 2005, A&A, 434, 785

Debes, J. H., Ge, J., Kuchner, M. J. Rogosky, M. 2004, ApJ, 608, 1095

Ford, V. G., Lisman, P. D., Shaklan, S. B., Trauger, J. T., Ho, T., Hoppe, D., & Lowman, A. E. 2004, Proc. SPIE, 5487, 1274

Kuchner, M. J. astro-ph/0401256

Kuchner, M. J., Crepp, J. R., Ge, J. 2005, ApJ, 628, 466 (KCG05)

Kuchner, M. J. & Spergel, D. N. 2003, ApJ, 594, 617

Kuchner, M. J. & Traub, W. A. 2002, ApJ, 570, 900

Lay, O. P., Green, J. J., Hoppe, D. L., Shaklan, S. B. 2005, Proc. SPIE, 5905, 148

Lloyd, J. P., Graham, J. R., Kalas, P., Oppenheimer, B. R., Sivaramakrishnan, A., Makidon, R., Macintosh, B. A., Max, C., Baudoz, P., Kuhn, J., & Potter, D. 2001, Proc. SPIE, 4490, 290

Lloyd, J. P. & Sivaramakrishnan, A. 2005, *ApJ*, 621, 1153

Lopez, B., Schneider, J., Danchi, W. C. 2005, *ApJ*, 627, 974

Lyot, B. 1939, *MNRAS*, 99, 580

Rouan, D. 2004, *EAS Publications Series*, 12, 21

Semaltianos, N. G. 2001, *Applied Surface Science*, 183, 223

Shaklan, S. B., & Green, J. J. 2005, *ApJ*, 628, 474 (SG05)

Sivaramakrishnan, A., Soummer, R., Sivaramakrishnan, A. V., Lloyd, J. P., Oppenheimer, B. R., & Makidon, R. B. 2005, *ApJ*, 634, 1416

Sivaramakrishnan, A., Koresko, C. D., Makidon, R. B., Berkefeld, T., Kuchner, M. J. 2001, *ApJ*, 552, 397

Trauger, J. et al. 2004, *Proc. SPIE*, 5487, 1330